Development of a Δ-Type Mobile Robot Driven by Three Standing-Wave-Type Piezoelectric Ultrasonic Motors

Juntian Zhou, Masaki Suzuki, Ryoma Takahashi, Kengo Tanabe, Yuki Nishiyama, Hajime Sugiuchi, *Member, IEEE*, Yusuke Maeda, *Member, IEEE*, and Ohmi Fuchiwaki, *Member, IEEE*

***Abstract*—We propose a new mobile robot that uses three standing-wave-type ultrasonic motors (USMs). The USMs are composed of two stacked-type piezoelectric actuators. Recently, with the miniaturization of electronic and microelectromechanical system devices and progress in the biomedical sciences, the demand for multifunctional manipulation of chip parts and biomedical cells has increased. Conventional multiaxial stages are too bulky for multifunctional manipulation in which multiple manipulators are required. Using conventional precise mobile robots is feasible for miniaturization of multifunctional manipulation, although their cables influence positioning repeatability. USMs are feasible actuators for realizing cableless robots because their energy efficiency is relatively higher than that of other motors of millimeter scale. The aim of this study is to develop a new type of omnidirectional mobile robot driven by USMs. In experiments, we evaluated the feasibility by investigating velocity, positioning deviation, and achieving repeatability of translational movements under open-loop control. We determine the repeatability as a ratio of the standard deviation of the final points to the average path length. The proposed mobile robot achieves velocities of 18.6–31.4 mm/s and repeatability of 4.1%–9.1% with a 200-g weight.**

***Index Terms*—Actuation and joint mechanisms, kinematics, mobile manipulation, mechanism design.**

I. Introduction

RECENTLY, with the miniaturization of electronic and microelectromechanical system devices and progress in the biomedical sciences, the demand for multifunctional manipulations of chip parts and biomedical cells has increased [1], [2]. Conventional multiaxial stages are too bulky for multifunctional manipulations in which multiple manipulators are required [3]. Meanwhile, lightweight and compact self-propelling robots have been under development; these include those using omni wheels [4], piezoelectric actuators as drivers [5], [6], shape memory alloys [7], and dielectric elastomers [8]. By mounting various tools on these robots and enabling cooperation with each other, it is possible to achieve compact multifunctional manipulations [9]. However, their speed decreases with the reduction in size, and their power supply requirements remain relatively high.

In our previous work, an inchworm miniature robot using piezoelectric actuators and electromagnets was developed. The robot had advantages such as high positioning resolutions of 10 nm, a light weight of 100 g, and a small size of 86 $\times$ 86 $\times$ 11 mm^3. Some practical applications of tiny sphere and biocell multifunctional manipulations have been demonstrated using this robot [10]–[12].

However, the robot also has a low speed of 7.3 mm/s and a power consumption of 31 W. That high power requirement has been difficult to achieve with noncontact power supply technologies [13], [14]. Moreover, the robot can only be driven on a well-polished ferromagnetic surface. These factors hinder its application.

Ultrasonic motors (USMs) are feasible actuators for overcoming these shortcomings because their energy efficiency is relatively higher than that of other motors of millimeter scale, although there are no published reports on omnidirectional mobile robots using USMs thus far [15], [16].

In this study, we propose a new mobile robot driven by three standing-wave-type USMs, aiming at higher movement speed, lower power consumption suitable for a cableless power supply, and movement on a nonmagnetic surface.

In Section II, we explain the structure, driving principle, and fabrication of the robot. In Section III, we describe the modeling and input signals for the fabricated robot. In Section IV, we evaluate the velocity and positioning repeatability of orthogonal movements of the robot with and without the loads of 100 and 200 g. In Section V, we summarize the achievements of this study and discuss future work.

II. Δ-type Mobile Robot Driven by Three USMs

Fig. 1 shows the newly proposed robot. It consists of a three standing-wave-type linear USMs (P-661, PI), an equilateral-triangle-shaped main stage, three substages blocks, and three pairs of parallel leaf springs. The specifications are given in

Manuscript received February 23, 2020; accepted July 8, 2020. Date of publication August 19, 2020; date of current version August 27, 2020. This letter was recommended for publication by Associate Editor K. Tahara and Editor P. Rocco upon evaluation of the Reviewers' comments. This work was partially supported by Murata Science Foundation. *(Corresponding author: Ohmi Fuchiwaki.)*

The authors are with the Department of Mechanical Engineering, Yokohama National University, Yokohama 240-8501, Japan (e-mail: zhou-juntian-bp@ynu.jp; suzuki-masaki-dj@ynu.jp; takahashi-ryoma-pc@ynu.jp; kengo-tanabe-hy@ynu.jp; nishiyama-yuki-dt@ynu.jp; sugi@ynu.ac.jp; maeda@ynu.ac.jp; ohmif@ynu.ac.jp).

This letter has supplementary downloadable material available at https://ieeexplore.ieee.org, provided by the authors.

Digital Object Identifier 10.1109/LRA.2020.3018031

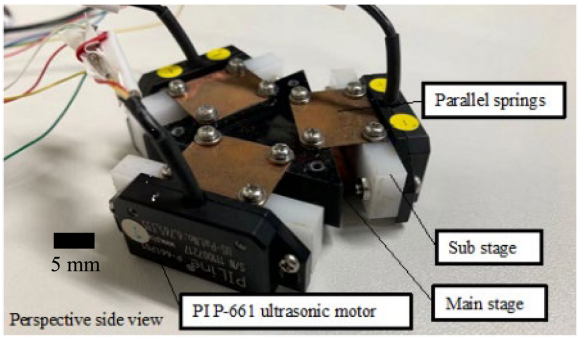

Fig. 1. Perspective view of a Δ-type mobile robot driven by three USMs.

TABLE I
SPECIFICATIONS OF THE PI P-661 ULTRASONIC MOTOR (DETAILED SPECIFICATIONS ARE SHOWN IN THE SUPPORTING INFORMATION)

Physical Quantity	Value
Travel range	1.5 m (restricted by the length of frictional bar)
Resolution (open loop)	0.05 μm
Maximum velocity	500 mm/s
Resonant frequency	210 kHz
Power source (DC)	12 V
Maximum output power	5 W
Mass	10 g
Dimensions	14 × 35 × 6 mm

TABLE II
COMPARISON OF SPECIFICATIONS AMONG PRECISE MOBILE ROBOTS (ESTIMATING METHODS OF POWER ARE SHOWN IN THE SUPPORTING INFORMATION)

Physical Quantity	Proposed Robot	Previous Robot [14]	MiCRoN [10]
Principle	Resonance drive	Inchworm	Stick slip
Max. speed [mm/s] (Power [W]) {Input voltage to PZT}	31.5 (4) {60 V_{pp}, 210 kHz, sine}	7.3 (31) {120 V_{pp}, 125 Hz, sine}	2 (no data) {400 V_{pp}, 1.5 kHz, sawtooth}
Resolution [μm]	0.05	0.01	0.002
Range [cm^2]	>50 × 50		
Repeatability [%] (Ratio of SD of final points to path length under open-loop control)	3–15	2–3	no data
Mass [g]	45	100	12
Dimensions [mm^3]	55 × 55 ×14	86 × 86 × 11	12 x 12 x 17.5
Power [W] for 2 mm/s { voltage to PZT}	1 or less {60 V_{pp}, 210 kHz, sine, duty ratio = 7%}	29 {120 V_{pp}, 33 Hz, sine}	no data (400 V_{pp}, 1.5 kHz, sawtooth)

Table I, with additional details provided in Section S1 in the Supporting Information. Each USM is fixed to its corresponding substage, where its altitude can be adjusted. Each side of the main stage is linked to the three substages through a pair of parallel leaf springs. Our design enabled the insertion of an additional tool in the main stage.

The specifications of the proposed robot are compared with those of conventional precise mobile robots in Table II. We also estimated their energy consumption for speeds of 2 mm/s in this table. We see that the proposed robot requires much lower power and also generates higher speed than the inchworm [14] and the stick-slip [10] based robots, as explained in Section S2 in the Supporting Information.

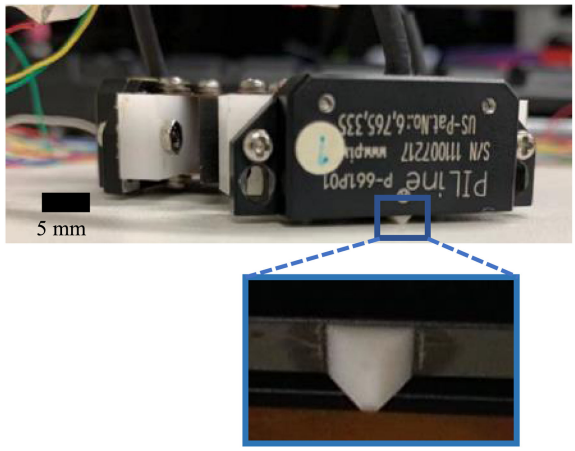

Fig. 2. Side view of the robot and close-up view of the friction tip from the bottom.

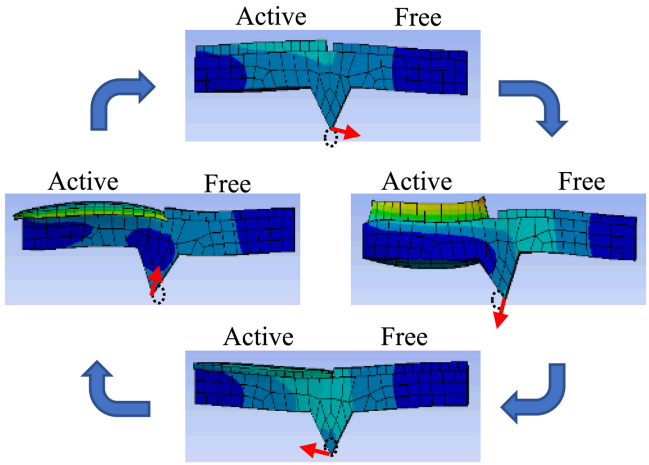

Fig. 3. Finite element method results of the diagonal motions of the friction tip.

As shown in Fig. 2, the friction tips of the three USMs are designed to be in direct contact with the surface. When driving the robot, the tips need to be placed on a smooth surface.

Fig. 3 shows that one of the piezo elements inside the motor generates the standing wave vibration and that the friction tips of the motors vibrate in an approximately diagonal manner. The friction tips scratch the surface and push the motor to the right. If the activated piezo element is switched to another, the tip pushes the motor leftward.

Each USM is controlled by an analog voltage from –10 V to +10 V input to the corresponding resonant circuit (C-184.161, PI), which generates the resonant frequency; the amplitude displacement and driving direction are adjusted by the analog input voltage.

As shown in Fig. 4, the frictional forces are oriented 120° from each other and have an offset r referring to the center of the robot. By properly changing the three input analog voltages, the composite vector of the three frictional force vectors can be oriented in any direction and simultaneously produce a

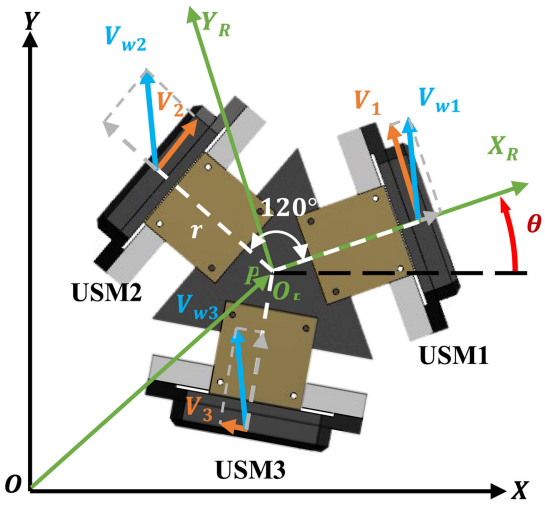

Fig. 4. Kinematic model of the Δ-type robot.

moment for rotation on the surface; the robot can thereby realize holonomic driving properties [6], [9]–[13].

III. Kinematics

Fig. 4 shows the kinematic model of the Δ-type mobile robot. We define the three USMs as USM1, USM2, and USM3 in the counterclockwise (CCW) direction. The center of the robot's frame is the center of mass of the robot. We determined that X_R, the axis of the robot frame, is perpendicular to the driving direction on USM1. θ denotes the orientation of the robot and is positive in the CCW direction.

For each USM, its position with respect to the robot frame can be described by multiplying the rotation matrix and the distance r from the center of the robot using the following equation:

$$P_i = \begin{bmatrix} x_i \\ y_i \end{bmatrix} = \boldsymbol{R}(\alpha_i) \cdot r \begin{bmatrix} 1 \\ 0 \end{bmatrix}$$

where

$$\boldsymbol{R}(\theta) = \begin{bmatrix} \cos(\theta) & -\sin(\theta) \\ \sin(\theta) & \cos(\theta) \end{bmatrix}.$$

We thus have

$$\boldsymbol{P}_1 = r \begin{bmatrix} 1 \\ 0 \end{bmatrix}, \quad \boldsymbol{P}_2 = \tfrac{1}{2} r \begin{bmatrix} -1 \\ \sqrt{3} \end{bmatrix}, \quad \boldsymbol{P}_3 = \tfrac{-1}{2} r \begin{bmatrix} 1 \\ \sqrt{3} \end{bmatrix}. \quad (1)$$

The unit direction vector of the translation direction $\boldsymbol{D_i}$ of each USM is perpendicular to its position vector $\boldsymbol{P_i}$. Therefore, $\boldsymbol{D_i}$ can be described as follows:

$$\boldsymbol{D_i} = \boldsymbol{R}\left(\frac{\pi}{2}\right) \frac{\boldsymbol{P_i}}{|\boldsymbol{P_i}|} = \frac{1}{r} \boldsymbol{R}\left(\frac{\pi}{2}\right) \boldsymbol{P_i},$$

from which we can obtain

$$\boldsymbol{D}_1 = \begin{bmatrix} 0 \\ 1 \end{bmatrix}, \quad \boldsymbol{D}_2 = \tfrac{-1}{2} \begin{bmatrix} \sqrt{3} \\ 1 \end{bmatrix}, \quad \boldsymbol{D}_3 = \tfrac{1}{2} \begin{bmatrix} \sqrt{3} \\ -1 \end{bmatrix}. \quad (2)$$

According to the coordinate transformation equation, where $\boldsymbol{x}$ represents the coordinate in world frame, $\boldsymbol{P}$ represents the coordinate in the robot frame with respect to the world frame, and $\boldsymbol{x'}$ denotes the coordinate in the robot frame,

$$\boldsymbol{x} = \boldsymbol{p} + \boldsymbol{R}(\theta)\, \boldsymbol{x'}. \quad (3)$$

The position of each USM can then be derived from

$$\boldsymbol{P_{wi}} = \boldsymbol{P} + \boldsymbol{R}(\theta)\, \boldsymbol{P_i},$$

and we can obtain the components as follows:

$$\boldsymbol{P}_{w1} = \begin{bmatrix} x + r \cdot \cos(\theta) \\ y + r \cdot \sin(\theta) \end{bmatrix}, \boldsymbol{P}_{w2} = \begin{bmatrix} x - r \cdot \cos\left(\theta - \frac{1}{3}\pi\right) \\ y - r \cdot \sin\left(\theta - \frac{1}{3}\pi\right) \end{bmatrix},$$

$$\boldsymbol{P}_{w3} = \begin{bmatrix} x + r \cdot \cos\left(\theta - \frac{2}{3}\pi\right)) \\ y + r \cdot \sin\left(\theta - \frac{2}{3}\pi\right) \end{bmatrix}. \quad (4)$$

When we differentiate $\boldsymbol{P_{wi}}$ of each USM in (4), we obtain $\boldsymbol{V_{wi}}$, the velocity of $\boldsymbol{P_{wi}}$ with respect to the world frame, as

$$\boldsymbol{V_{wi}} = \dot{\boldsymbol{P}}_{\boldsymbol{wi}} = \dot{\boldsymbol{P}} + \dot{\boldsymbol{R}}(\boldsymbol{\theta})\, \boldsymbol{P_i}. \quad (5)$$

$\boldsymbol{V_{wi}}$ is the sum of the translation direction of the robot and the velocity determined by the rotational motion. Substituting (1) into (5), we can obtain $\boldsymbol{V_{wi}}$ as follows:

$$\boldsymbol{V}_{w1} = \begin{bmatrix} \dot{x} - r \cdot \dot{\theta} \sin(\theta) \\ \dot{y} + r \cdot \dot{\theta} \cos(\theta) \end{bmatrix}, \boldsymbol{V}_{w2} = \begin{bmatrix} \dot{x} + r \cdot \dot{\theta} \sin\left(\theta - \frac{1}{3}\pi\right) \\ \dot{y} - r \cdot \dot{\theta} \cos\left(\theta - \frac{1}{3}\pi\right) \end{bmatrix},$$

$$\boldsymbol{V}_{w3} = \begin{bmatrix} \dot{x} - r \cdot \dot{\theta} \sin\left(\theta - \frac{2}{3}\pi\right) \\ \dot{y} + r \cdot \dot{\theta} \cos\left(\theta - \frac{2}{3}\pi\right) \end{bmatrix}. \quad (6)$$

Although USMs should generate velocity in any direction equal to $\boldsymbol{V_{wi}}$, they generate velocity in a constant direction with respect to the robot frame. Here, we approximate that their generated velocities are equal to the inner product of the unique direction and the translation direction of the robot.

In other words, we approximate that the USMs generate frictional force only in the driving direction because the frictional force in the perpendicular direction should be minimized to prevent unexpected vibrations and positioning errors from being generated. We investigate the modeling error of this approximation of the anisotropic friction in the next section.

By applying the estimation mentioned above, the translational velocities of the USMs with respect to the robot frame can then be obtained from the following equation:

$$\boldsymbol{V_i} = \boldsymbol{V_{wi}}^T \cdot (\boldsymbol{R}(\theta)\, \boldsymbol{D_i}). \quad (7)$$

By substituting (6) into (7), each USM's translational velocity can be obtained:

$$\begin{bmatrix} V_1 \\ V_2 \\ V_3 \end{bmatrix} = \begin{bmatrix} -\sin(\theta) & \cos(\theta) & r \\ \sin\left(\theta - \frac{\pi}{3}\right) & -\cos\left(\theta - \frac{\pi}{3}\right) & r \\ \sin\left(\theta + \frac{\pi}{3}\right) & -\cos\left(\theta + \frac{\pi}{3}\right) & r \end{bmatrix} \cdot \begin{bmatrix} \dot{x} \\ \dot{y} \\ \dot{\theta} \end{bmatrix}, \quad (8)$$

where $\dot{x}$, $\dot{y}$, and $\dot{\theta}$ represent the translational and rotation angular speeds of the robot mass center, respectively, with respect to the world frame.

By applying the inverse matrix, we represent the robot's three velocity components, $\dot{x}$, $\dot{y}$, and $\dot{\theta}$, by the three velocities of the

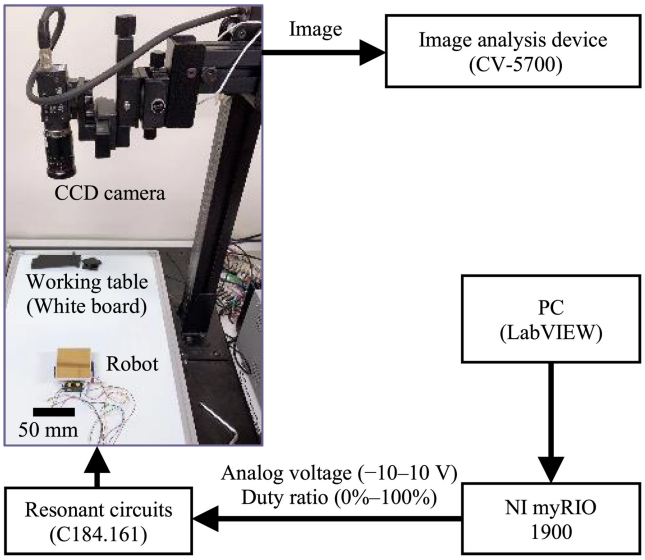

Fig. 5. Experimental setup.

USMs, V_1, V_2, and V_3 as given by

$$\begin{bmatrix} \dot{x} \\ \dot{y} \\ \dot{\theta} \end{bmatrix} = \begin{bmatrix} \frac{-2}{3}\sin(\theta) & \frac{-2}{3}\sin\left(\frac{\pi}{3}-\theta\right) & \frac{2}{3}\sin\left(\frac{\pi}{3}+\theta\right) \\ \frac{2}{3}\cos(\theta) & \frac{-2}{3}\cos\left(\frac{\pi}{3}-\theta\right) & \frac{-2}{3}\cos\left(\frac{\pi}{3}+\theta\right) \\ \frac{1}{3r} & \frac{1}{3r} & \frac{1}{3r} \end{bmatrix} \times \begin{bmatrix} V_1 \\ V_2 \\ V_3 \end{bmatrix}. \quad (9)$$

Because the resonant frequency of each USM is a unique value and the amplitude displacements are adjusted by the corresponding analog input voltages, the USMs' velocities of V_1, V_2, and V_3 are also adjustable by the input voltages from -10 to 10 V. We determined the theoretical ratio of the input analog voltages from the ratio of V_1, V_2, and V_3 from (9) in the experiments with their maximum input voltages of 5 V, as explained in Section S5 in the Supporting Information.

IV. Experiments

To test the positioning property of the newly developed Δ-type robot, an open-loop control experiment was conducted. An image analysis system, as shown in Fig. 5, was used to record the track of the robot. This system is composed of a low-distortion lens (CA-LHR8, Keyence), a digital CCD camera (CV-H500M, Keyence), an image analysis device (CV-5700, Keyence), a portable reconfigurable input–output device (myRIO-1900, NI), and a personal computer running LabVIEW. We chose a commercially available whiteboard after trying various materials to optimize the roughness of the ground surface. One of the main purposes of this study is to investigate the range of repeatability of the proposed mobile robot on a reasonable floor for expanding the applications. The coefficients of static and kinetic friction between the board and the robot were measured as 0.17 ± 0.2 and 0.072 ± 0.004 (average $\pm$ standard deviation), respectively, using the inclined surface method, as detailed in Tables S3 and S4-2 in the Supporting Information. We confirmed that the USMs were vibrating slightly from electromagnetic noise even when the control voltage was 0 V. This electromagnetic noise affected the USMs because we cut the shield cables to decrease the cable tensions, as explained in Section S4 in the Supporting Information.

TABLE III
Experimental Conditions

Working table	White board
Coefficient of static friction between the table and the robot with no weight	0.17 ± 0.2 (Average $\pm$ σ)
Coefficient of kinetic friction between the table and the robot with no weight	0.072 ± 0.004 (Average $\pm$ σ)
Initial attitude angle of the robot	$\theta = 0^{\circ}$
Duration per track	5 s
Measuring frequency	10 Hz
Search range of camera	2413 × 2049 pixels
Pixels per mm	8.9 pixels/mm
Recorded tracks per direction	10 tracks
Movements for a load-free group	12 translational directions (ϕ = 0°–330° in 30° increments), 2 rotational directions (CW, CCW)
Movements for load-weighted groups	4 translational directions (ϕ = 0°, 90°, 180°, 270°)

We supposed that the very low kinetic friction under the condition of slight vibration is one of the main reasons why the robot realizes omnidirectional mobility.

The experiment was separated into a weight-loaded group and a load-free group. The steps of the experiment were as follows:

1) Load the weight on the robot.
2) Adjust the robot's location and attitude angle.
3) Manually adjust the theoretical ratio of the input voltages until the movement direction of the robot is close to the target direction (see Tables S5-1, S5-2, and S5-3 in the Supporting Information).
4) Move the robot for 10 s by measuring the track using the image analysis device.
5) Repeat 10 times from Step 4.
6) Repeat from Step 2 for each movement (12 translations and 2 rotations for the load-free group and 4 translations for the weighted group, respectively).
7) Calculate the repeatability from the obtained data.

In this study, we determined the repeatability as the ratio of the standard deviation of the final points to the average path length. The experimental conditions are listed in Table III. We defined ϕ as the direction of the translational motions.

V. Experimental Results

A. Translational Movement of the Load-free Group

Fig. 6 shows the tracks of translational movements. The dotted blue lines show the 12 directions. The red points are the average arrival points of each direction. The deviation bars represent the corresponding standard deviations on the x and y axes of the average arrival points.

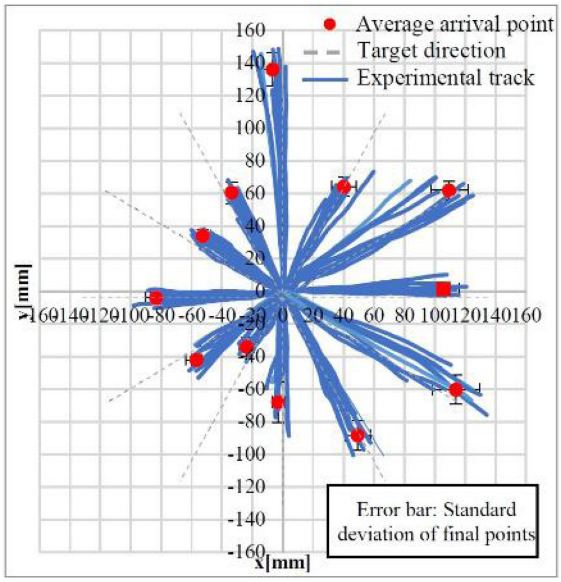

Fig. 6. Trajectories of translational movements with no weight.

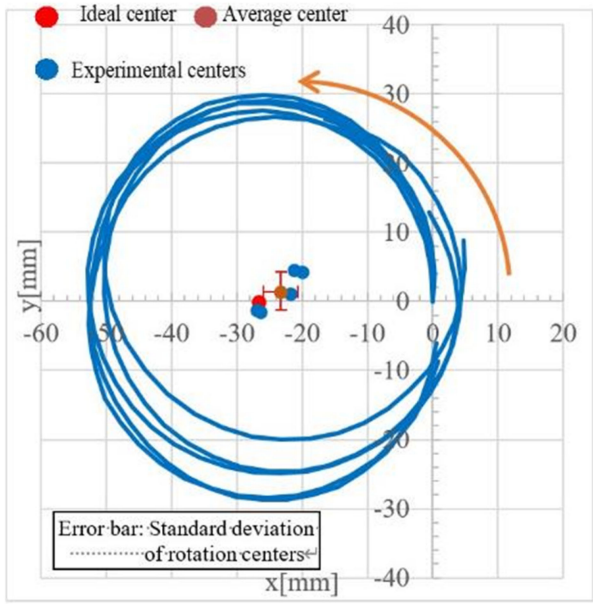

Fig. 7. Trajectories of CCW rotation with no weight.

We found that the translational tracks significantly deviate from their target directions. The standard deviation of the distances from the final to the average arrival points is distributed from 6 to 17 mm. We concluded that the distribution is mainly caused by nonuniformity of the number of frictional tips contacting the floor simultaneously (as discussed in Section S6 of the Supporting Information), the tension of the cables, and the nonuniformity of the frictional condition of the working surface. These factors especially affect fluctuation of the attitude angle θ.

B. Rotational Motion of the Load free Group

Figs. 7 and 8 show the rotational tracks of an offset mark on the robot in clockwise (CW) and CCW directions, respectively. Blue lines are tracks. The red points represent the ideal rotation centers. Brown points represent average centers. Deviation bars show the standard deviation of the experimental rotation centers (blue points) from the average rotation center.

The average rotation speed reached 144°/s. The standard deviations of the rotation centers form the average rotation center were 3.9 and 4.3 mm in the CCW and CW directions, respectively. The circles of rotation were also not properly closed. We suspect that the unevenness of the frictional condition and cable tension may be responsible for this.

C. Translational Motion of the Loaded Group

The Δ-type robot is designed to work by applying manipulators for microscopic operations. Therefore, it is necessary to investigate the positioning property when it is loaded with additional weight.

Fig. 9 shows the image of the Δ-type robot loaded with a weight. We moved the robot with two different weights of 100 and 200 g, whose tracks are shown in Figs. 10 and 11, respectively. The blue lines show the tracks in four orthogonal

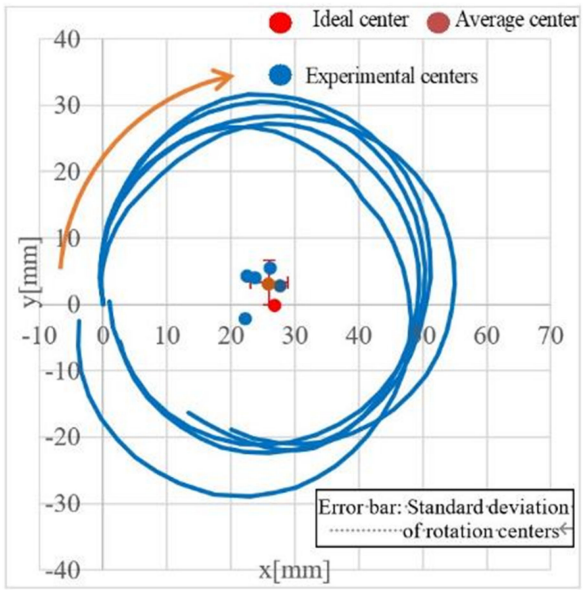

Fig. 8. Trajectories of CW rotation with no weight.

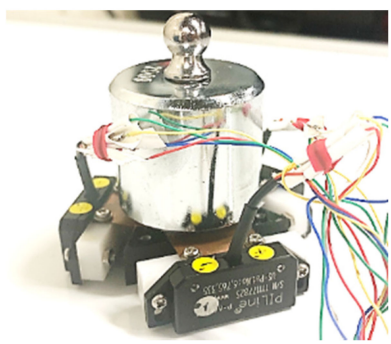

Fig. 9. Δ-type robot mounted with a weight.

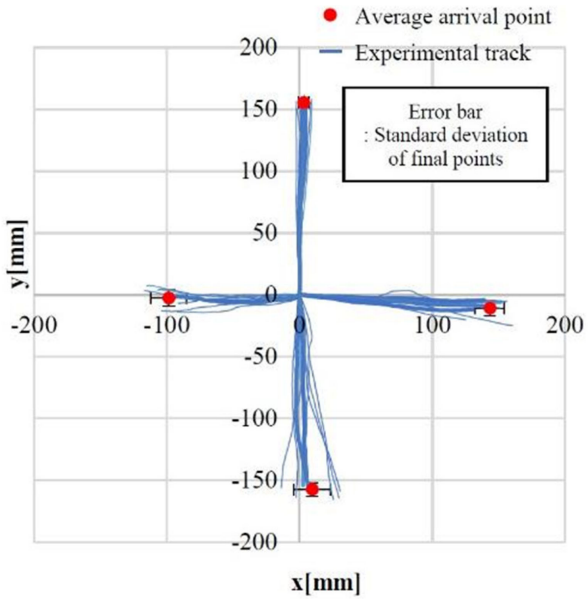

Fig. 10. Tracks with a 100-g weight in orthogonal directions.

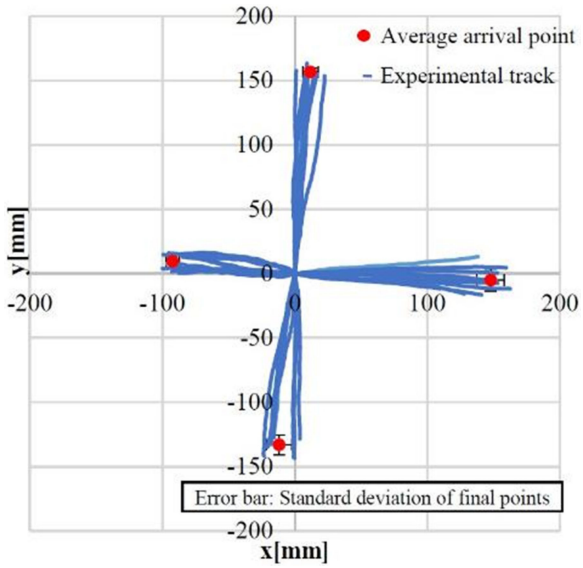

Fig. 11. Tracks with a 200-g weight in orthogonal directions.

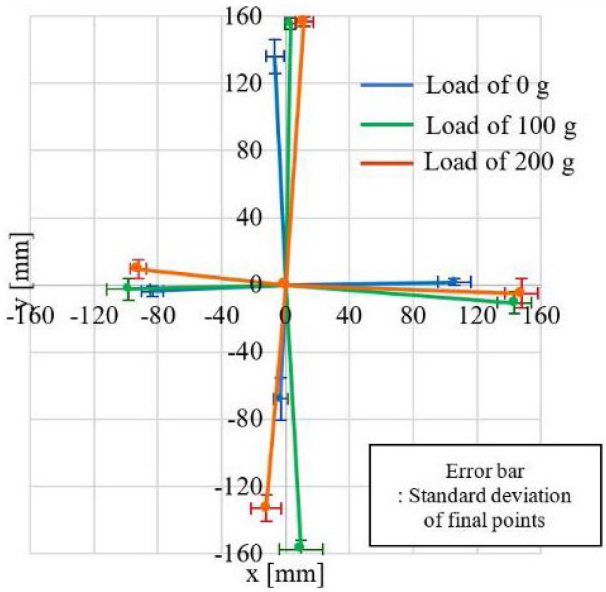

Fig. 12. Comparison of average track lengths and deviations of the final points among loads of 0, 100, and 200 g.

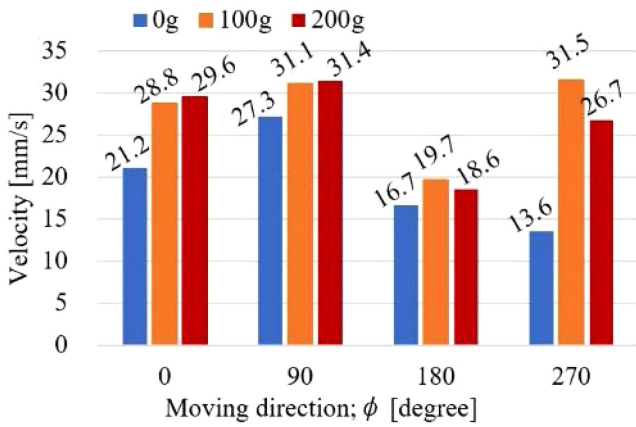

Fig. 13. Comparison of velocities in four directions with 0, 100, and 200g.

directions. The red points are the average arrival points for each direction. The deviation bars represent standard deviations of final arrival point in the x and y axes from the average arrival points. The standard deviation in the 100-g group ranged from 4 to 15 mm, and that in the 200-g group ranged from 6 to 12 mm.

D. Comparison of Positioning Properties

Fig. 12 shows a comparison of the average track lengths of the three groups in four directions. It can be observed that, in all four directions, the robot ran a distance of 20 mm longer when it was loaded with weight in the same time period. Especially, in the $-y$ direction, when the robot was loaded with weight, the distance became more than doubled compared to that of the nonweight group.

Fig. 13 depicts the differences in average velocities among the conditions tested. The velocities increased by 2–18 mm/s when the robot was loaded with weight. A reasonable amount of weight increases the velocity because the frictional conditions between each frictional tip and the working surface improve.

We concluded that the difference of the average final points among those experiments was likely caused by the systematic errors resulting from the cable tension and the difference of load distribution among the three friction tips.

Fig. 14 shows a comparison of the repeatabilities among the three groups. The repeatability is basically 2%–10% higher in the groups with weight loading. This is because the weight provides the friction tips of the motors better contact with the working surface and reduces slips during the movement.

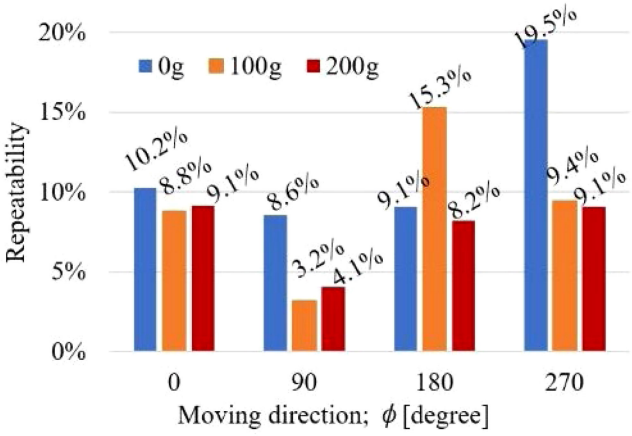

Fig. 14. Comparison of the repeatabilities in four directions with 0, 100, and 200 g. (The repeatability is determined as a ratio of the standard deviation of the final points to the average path length.)

VI. Conclusion and Future Prospects

In this study, we constructed a prototype robot using standing-wave-type USMs. In a load-free experiment, the robot realized omnidirectional movement on a commercially available whiteboard. It reached a maximum translational speed of 27.3 mm/s. The positioning repeatability was distributed from 8.6% to 19.5%. Large deviations and low repeatability are considered mainly to result from the nonuniformity of the number of frictional tips contacting the floor simultaneously, the tension of the cables, and the nonuniformity of the frictional condition of the working surface. Those factors especially affect fluctuation of the attitude angle θ.

In comparison experiments, we found that, by loading a reasonable weight of 100-g on the robot, the speed could be increased from 13.6 to 31.5 mm/s. We also confirmed that the repeatability is distributed from 4.1% to 9.1% with the 200-g weight. This means that the proposed robot can feasibly be used for efficient manipulations and positions with 200-g of manipulators.

In future work, we plan to increase the number of friction tips to improve the repeatability, as explained in Section S6 in the Supporting Information. We also plan to realize motion compensation and feedback control, which will improve the precision and repeatability of the robot and is necessary for applications requiring automatic control. We also plan to introduce cableless technology. This will improve compactness and repeatability of the robot because it removes the effect of cable tension. Furthermore, we plan to conduct experiments to check the effect of decreasing the surface roughness and the flatness error on repeatability because these are also considered to be responsible for the deviation. Finally, we plan to measure the positioning properties on the submicrometer scale with an $XY\theta$ position sensor organized by four encoders [17]. We will also develop a servo control method with submicrometer resolution to test the robot's ability for precise operations.

Feasible applications of the proposed robot include assembly of chip parts; biomedical applications; and wide area flexible positioning of lightweight tools, sensors, and manipulators where versatility and cable-free operation are required.

References

[1] W. Hagiwara, T. Ito, K. Tanaka, R. Tokui, and O. Fuchiwaki, "Capillary force gripper for complex-shaped micro-objects with fast droplet forming by on-off control of a piston slider," *IEEE Rob. Autom. Lett.*, vol. 4, no. 4, pp. 3695–3702, Jul. 2019.

[2] T. Chen, L. Sun, L. Chen, W. Rong, and X. Li, "A hybrid-type electrostatically driven microgripper with an integrated vacuum tool," *Sens. Actuators, A*, vol. 158, pp. 320–327, Mar. 2010.

[3] H. Xie and S. Régnier, "Development of a flexible robotic system for multiscale applications of micro/nanoscale manipulation and assembly," *IEEE/ASME Trans. Mechatron.*, vol. 16, no. 2, pp. 266–276, Apr. 2011.

[4] F. Tajti, G. Szyayer, B. Kovacs, and P. Korondi, "Robot base with holonomic drive," *Proc. IFAC*, vol. 47, No. 3, pp. 5715–5720, Aug. 2014.

[5] N. A. Saadabad, H. Moradi, and G. Vossoughi, "Dynamic modeling, optimized design, and fabrication of a 2DOF piezo-actuated stick-slip mobile microrobot," *Mech. Mach. Theory*, vol. 133, pp. 514–530, Mar. 2019.

[6] S. M. Martel, C. O. Lorenzo, B. C. F. Juan, R. Stefen, K. Torsen, and S. Jeremy, "General description of the wireless miniature NanoWalker robot designed for atomic-scale operations," *Proc. SPIE*, vol. 4568, pp. 231–240, Oct. 2001.

[7] X. Huang, K. Kumar, M. K. Jawed, A. M. Nasab, Z. Y. W. Shan, and C. Majidi, "Chasing biomimetic locomotion speeds: Creating untethered soft robots with shape memory alloy actuators," *Sci. Rob.* vol. 3, no. 25, Dec. 2018, Art. no. eaau7557.

[8] X. Ji. X. Liu *et al.*, "An autonomous untethered fast soft robotic insect driven by low-voltage dielectric elastomer actuators," *Sci. Rob.* vol. 4, no. 37, Dec. 2019, Art. no. eaaz6451.

[9] S. Fatikow, *Automated Nanohandling by Microrobots*. New York, NY, USA: Springer, 2008.

[10] W. Driesen, T. Varidel, S. Regnier, and J.-M. Breguet, "Micro manipulation by adhesion with two collaborating mobile micro robots," *J. Micromech. Microeng.*, vol. 15, S259–S267, Sep. 2005.

[11] O. Fuchiwaki, Y. Tanaka, and T. Hyakutake, "Multi-axial non-contact in situ micromanipulation by steady streaming around two oscillating cylinders on holonomic miniature robots," *Microfluid. Nanofluid.*, vol. 22, no. 80, Jul. 2018. doi: 10.1007/s10404-018-2098-5.

[12] O. Fuchiwaki, A. Ito, D. Misaki, and H. Aoyama, "Multi-axial micromanipulation organized by versatile micro robots and micro tweezers," in *Proc. Int. Conf. Robot. Autom.*, Jun. 2008, pp. 893–898.

[13] O. Fuchiwaki, "Insect-sized holonomic robots for precise, omnidirectional, and flexible microscopic processing," *Pericion Eng.*, vol. 37, no. 1, pp. 88–106, Jan. 2013.

[14] O. Fuchiwaki, M. Yatsurugi, and T. Sato, "The basic performance of a miniature omnidirectional 6-legged inchworm robot from cm- to μm-scale precise positioning," *Trans. Mater. Res. Soc. Jpn.*, vol. 39, no. 2, pp. 211–215, Jan. 2014.

[15] K. Takemura, Y. Ohno, and T. Maeno, "Design of a plate type multi-DOF ultrasonic motor and its self-oscillation driving circuit," *Trans. Mater. Res. Soc. Jpn.*, vol. 9, no. 3, pp. 474–480, Sep. 2004.

[16] Y. Liu, J. Yan, L. Wang, and W. Chen, "A two-DOF ultrasonic motor using a longitudinal–bending hybrid sandwich transducer," *IEEE Trans. Ind. Electron.*, vol. 66, no. 4, pp. 3041–3050, Apr. 2019.

[17] O. Fuchiwaki, M. Yatsurugi, and A. Ogawa, "Design of an integrated 3DoF inner position sensor and 2DoF feedforward control for a 3DoF precision inchworm mechanism, in *Proc. Int. Conf. Robot. Autom.*, May 2013, pp. 5475–5481.